

## PORT DOCUMENTATION PAGE

AD-A211 180

IC

CTE

D

D

D

D

D

D

D

D

D

D

D

D

D

D

D

D

D

D

D

D

D

D

D

D

D

D

D

D

D

D

D

D

D

D

D

D

1b. RESTRICTIVE MARKINGS

3. DISTRIBUTION/AVAILABILITY OF REPORT

Approved for public release;  
distribution unlimited.

2b. DECLASSIFICATION/DOWNGRADING SCHEDULE

SCA 08 1989

4. PERFORMING ORGANIZATION REPORT NUMBER(S)

5. MONITORING ORGANIZATION REPORT NUMBER(S)

ARO 25575-5-EG-5

6a. NAME OF PERFORMING ORGANIZATION  
JAI Associates, Inc.6b. OFFICE SYMBOL  
(if applicable)

7a. NAME OF MONITORING ORGANIZATION

U. S. Army Research Office

6c. ADDRESS (City, State, and ZIP Code)

P. O. Box 293, Mountain View, GA 94042

7b. ADDRESS (City, State, and ZIP Code)

P. O. Box 12211  
Research Triangle Park, NC 27709-22118a. NAME OF FUNDING/SPONSORING  
ORGANIZATION

U. S. Army Research Office

8b. OFFICE SYMBOL  
(if applicable)

9. PROCUREMENT INSTRUMENT IDENTIFICATION NUMBER

DAA603-88-C-0006

8c. ADDRESS (City, State, and ZIP Code)

P. O. Box 12211  
Research Triangle Park, NC 27709-2211

10. SOURCE OF FUNDING NUMBERS

PROGRAM ELEMENT NO.	PROJECT NO.	TASK NO.	WORK UNIT ACCESSION NO.

11. TITLE (Include Security Classification)

Unsteady Interaction of a Rotor with a Vortex, AIAA Paper AIAA-89-1848

12. PERSONAL AUTHOR(S)

G. R. Srinivasan &amp; W. J. McCroskey

13a. TYPE OF REPORT  
Reprint13b. TIME COVERED  
FROM TO

14. DATE OF REPORT (Year, Month, Day)

15. PAGE COUNT

16. SUPPLEMENTARY NOTATION

The view, opinions and/or findings contained in this report are those of the author(s) and should not be construed as an official Department of the Army position, policy, or decision, unless so designated by other documentation.

17. COSATI CODES

FIELD	GROUP	SUB-GROUP

18. SUBJECT TERMS (Continue on reverse if necessary and identify by block number)

Unsteady; Euler &amp; Navier-Stokes, Parallel and Oblique Blade-Vortex Interaction

19. ABSTRACT (Continue on reverse if necessary and identify by block number)

The unsteady, three-dimensional flow field of a helicopter rotor blade encountering a passing vortex is calculated by solving the Euler/thin layer Navier-Stokes equations by a finite-difference numerical procedure. A prescribed vortex method is adopted to preserve the structure of the interacting vortex. The cases considered for computation correspond to the experimental model rotor test conditions of Caradonna et al. and consist of parallel and oblique interactions. Comparison of the numerical results with test data show good agreement for both parallel and oblique interactions at subsonic and transonic tip speeds.

89

20. DISTRIBUTION/AVAILABILITY OF ABSTRACT

 UNCLASSIFIED/UNLIMITED
  SAME AS RPT.
  DTIC USERS

Unclassified

22a. NAME OF RESPONSIBLE INDIVIDUAL

22b. TELEPHONE (Include Area Code)

22c. OFFICE SYMBOL



**AIAA-89-1848**

**UNSTEADY INTERACTION  
OF A ROTOR WITH A VORTEX**

G. R. Srinivasan,

JAI Associates, Inc., Sunnyvale, CA

W. J. McCroskey,

U. S. Army Aeroflightdynamics Directorate-AVSCOM,

NASA Ames Research Center, Moffett Field, CA

Accession For	
NTIS	CRA&I
DTIC	TAB
Unannounced	
Justification	
By	
Distribution /	
Availability Codes	
Dist	Avail and/or Special
A-120	



**AIAA 20th Fluid Dynamics, Plasma Dynamics  
and Lasers Conference**

Buffalo, New York / June 12-14, 1989

# UNSTEADY INTERACTION OF A ROTOR WITH A VORTEX

G. R. Srinivasan \*

JAI Associates Inc., Kifer Court, Sunnyvale, California

W. J. McCroskey \*\*

U. S. Army Aeroflightdynamics Directorate -AVSCOM

NASA Ames Research Center, Moffett Field, California

## Abstract

The unsteady, three-dimensional flow field of a helicopter rotor blade encountering a passing vortex is calculated by solving the Euler/thin layer Navier-Stokes equations by a finite-difference numerical procedure. A prescribed vortex method is adopted to preserve the structure of the interacting vortex. The cases considered for computation correspond to the experimental model rotor test conditions of Caradonna et al.<sup>2,3</sup> and consist of parallel and oblique interactions. Comparison of the numerical results with test data show good agreement for both parallel and oblique interactions at subsonic and transonic tip speeds.

## Nomenclature

$a$	= speed of sound
$a_o$	= vortex core radius, see Eq. (6)
$a_\infty$	= free stream sound speed
$C$	= characteristic length scale, chord of the blade
$C_w$	= chord of the vortex generating wing
$C_p$	= pressure coefficient, based on local dynamic pressure
$e$	= total energy per unit volume
$\hat{F}, \hat{G}, \hat{H}$	= flux vectors
$J$	= Jacobian of the coordinate transformation
$M_\infty$	= free stream Mach number
$M_{tip}$	= tip Mach number of the rotor blade
$p$	= static pressure
$p_\infty$	= free stream pressure
$Pr$	= Prandtl number
$\hat{Q}$	= flowfield vector
$r$	= radial distance from the vortex center
$r_B$	= rotor reference station normalized by $R$
$R$	= rotor radius
$R(t)$	= rotational matrix, see Eq. (4)
$Re$	= Reynolds number
$\hat{S}$	= viscous flux vector
$u_\infty$	= free stream velocity
$u, v, w$	= velocity components

$v_\theta$	= tangential velocity of vortex
$U, V, W$	= contravariant velocity components
$x, y, z, t$	= inertial coordinates
$x_o, z_o$	= vortex offset position relative to rotor axis
$\bar{x}_v, \bar{z}_v$	= distance from blade leading edge to vortex
$\bar{x}, \bar{y}, \bar{z}, \bar{t}$	= blade attached coordinates
$\gamma$	= ratio of specific heats
$\Gamma$	= circulation for the vortex
$\hat{\Gamma}$	= dimensionless strength of the vortex, $\Gamma/(a_\infty C)$
$\mu$	= viscosity coefficient, advance ratio
$\xi, \eta, \zeta, \tau$	= generalized curvilinear coordinates
$\rho_\infty$	= free stream density
$\rho$	= density
$\psi$	= azimuth angle
$\Omega$	= angular velocity of the rotor

## Introduction

The accurate simulation of the flowfield of a helicopter rotor is still one of the most complex and challenging problems of applied aerodynamics. This is true in spite of the availability of the present day supercomputers of Cray-2 class and improved numerical algorithms. The flowfield of a rotor in forward flight is highly three-dimensional, unsteady and viscous, with pockets of transonic flow near the blade tips on the advancing side and regions of dynamic stall on the retreating blades. In addition, the blades also shed complex vortical wakes; the concentrated tip vortex of each blade generally passes close to the following blades. The close encounter of these (force free) concentrated vortices with the rotor blades is often the cause of unsteady load fluctuations and acoustic noise. Some of these complexities associated with the flowfield are delineated in a schematic of helicopter rotor in forward flight shown in Fig. 1.

The spiralling vortex sheet emanating from each of the blades of the rotor has a profound influence on the performance of the helicopter. It not only alters the effective pitch angle of the blades and thus the airloads, but also

Copyright © 1989 by the American Institute of Aeronautics and Astronautics, Inc. No copyright is asserted in the United States under Title 17, U.S. Code. The U.S. Government has a royalty-free license to exercise all rights under the copyright claimed herein for Governmental purposes. All other rights are reserved by the copyright owner.

\* Senior Research Scientist, Associate Fellow, AIAA.

\*\* Senior Staff Scientist, Associate Fellow, AIAA.

produces highly nonlinear interactions of the vortex with the rotor flowfield. It is possible that such interactions might produce vortex induced boundary layer separation which results in loss of lift and increased drag. An accurate simulation of the rotor flowfield, therefore, must consider the induced effects of the vortex wake including effects of blade-vortex interactions (BVI).

Numerical simulations of vortex wakes is being attempted only recently after bigger and faster computers have become available (see for example Ref. 1). These investigations have some limited success to date. On the other hand, much of the progress in modeling the blade-vortex interaction has been hampered by the lack of development of theoretical and/or numerical techniques to preserve the structure of the concentrated vortices in the flowfield without significant diffusion. The study of blade-vortex interaction has been the subject of numerous recent research papers.<sup>4-11</sup> These studies have considered different methods of preserving the concentrated vortex in the flowfield. Among these, the vortex-fitting technique (also called the split potential formulation in potential flow methods) has demonstrated to be a very effective method in preserving the vortex even when the grid density is sparse. This method has also proven very economical<sup>7,8</sup> compared to a more exact formulation used in Ref. 5.

The purpose of this study is to devise numerical methods for the solution of the Euler and Navier-Stokes equations to accurately calculate the flowfield of a helicopter rotor, including the effects of blade-vortex interactions. In particular, this paper concentrates on demonstrating the ability to calculate such an interaction flowfield for parallel and oblique blade-vortex interactions, which is three-dimensional and unsteady, on a model helicopter rotor tested in a wind tunnel by Caradonna et al.<sup>2,3</sup> Because these experiments were specifically conducted to provide test data to evaluate different numerical methods, the experimental apparatus was kept simple and consisted of rigid two-bladed rotor. The blades are made up of NACA 0012 airfoil and have rectangular planform with no twist or taper; the interacting vortex was generated upstream of the model rotor by means of a lifting rectangular wing mounted on the roof of the tunnel as shown in Fig. 2.

### Governing Equations and Numerical Scheme

The governing partial differential equations are the unsteady, Euler/thin layer Navier-Stokes equations. In this study, the thin layer Navier-Stokes code recently written specifically for helicopter rotor applications<sup>12</sup> will provide the starting point for further modifications to calculate the blade-vortex interaction flowfield. In order to

assess the importance of viscous effects in these interacting flowfields, both the Euler and thin layer Navier-Stokes equations are solved. The Euler calculations are performed by turning off the viscous terms in the Navier-Stokes equations set and appropriately modifying the surface boundary condition. The mathematical formulation presented in the following paragraphs is for the solution of thin layer Navier-stokes equations with the added feature of introducing a prescribed vortex.

For generality, the equations are transformed from the inertial Cartesian reference frame  $(x, y, z, t)$  to the arbitrary curvilinear space  $(\xi, \eta, \zeta, \tau)$  moving with the blade, while retaining strong conservation law-form to capture shock waves. The transformed equations, following Ref. 13, can be written as

$$\partial_\tau(\hat{Q} - \hat{Q}_0) + \partial_\xi(\hat{F} - \hat{F}_0) + \partial_\eta(\hat{G} - \hat{G}_0) + \partial_\zeta(\hat{H} - \hat{H}_0) = Re^{-1} \partial_\zeta \hat{S} \quad (1)$$

where

$$\hat{Q} = J^{-1} \begin{bmatrix} \rho \\ \rho u \\ \rho v \\ \rho w \\ e \end{bmatrix}, \quad \hat{F} = J^{-1} \begin{bmatrix} \rho U \\ \rho u U + \xi_x p \\ \rho v U + \xi_y p \\ \rho w U + \xi_z p \\ U(e + p) - \xi_t p \end{bmatrix}$$

$$\hat{G} = J^{-1} \begin{bmatrix} \rho V \\ \rho u V + \eta_x p \\ \rho v V + \eta_y p \\ \rho w V + \eta_z p \\ V(e + p) - \eta_t p \end{bmatrix}, \quad \hat{H} = J^{-1} \begin{bmatrix} \rho W \\ \rho u W + \zeta_x p \\ \rho v W + \zeta_y p \\ \rho w W + \zeta_z p \\ W(e + p) - \zeta_t p \end{bmatrix}$$

Here  $\hat{Q}$  is the unknown flowfield vector and  $\hat{Q}_0$  is the solution of the Euler equations for a prescribed line vortex aligned with the uniform free stream of Mach number,  $M_\infty$ , in the  $y$ -direction (see Fig. 2). The terms  $\hat{F}$ ,  $\hat{G}$ ,  $\hat{H}$  and  $\hat{F}_0$ ,  $\hat{G}_0$ ,  $\hat{H}_0$  represent the appropriate flux vectors for the two flows, respectively. The hat, represented by  $\hat{(\ )}$ , in Eq. (1) denotes quantities scaled by the Jacobian  $J$ , e.g.,  $\hat{Q} = J^{-1}Q$  etc. The contravariant velocity components  $U$ ,  $V$  and  $W$  are defined as

$$U = \xi_t + \xi_x u + \xi_y v + \xi_z w$$

$$V = \eta_t + \eta_x u + \eta_y v + \eta_z w$$

$$W = \zeta_t + \zeta_x u + \zeta_y v + \zeta_z w$$

In the present formulation,  $\xi$  lies in the spanwise direction,  $\eta$  is in the chordwise or wraparound direction, and  $\zeta$  is normal to the blade surface.

The viscous flux vector  $\widehat{S}$  is used in the limit of thin-layer approximation and is given by

$$\widehat{S} = J^{-1} \begin{bmatrix} 0 \\ \mu m_1 u_\zeta + (\mu/3)m_2 \zeta_x \\ \mu m_1 v_\zeta + (\mu/3)m_2 \zeta_y \\ \mu m_1 w_\zeta + (\mu/3)m_2 \zeta_z \\ \mu m_1 m_3 + (\mu/3)m_2 (\zeta_x u + \zeta_y v + \zeta_z w) \end{bmatrix}$$

where

$$\begin{aligned} m_1 &= \zeta_x^2 + \zeta_y^2 + \zeta_z^2 \\ m_2 &= \zeta_x u_\zeta + \zeta_y v_\zeta + \zeta_z w_\zeta \\ m_3 &= \frac{1}{2}(u^2 + v^2 + w^2)_\zeta + \kappa Pr^{-1}(\gamma - 1)^{-1}(a^2)_\zeta \end{aligned}$$

In this equation,  $a$  is the speed of sound,  $\kappa$  is the coefficient of thermal conductivity and  $\mu$  is the viscosity computed as the sum of laminar and turbulent contributions for a turbulent boundary layer. Sutherland's equation is used for laminar viscosity and the two-layer algebraic eddy viscosity model of Baldwin and Lomax<sup>19</sup> is used to calculate the turbulent eddy viscosity, after minor modifications to account for the moving blade surface. Also,  $J$  is the transformation Jacobian, whose inverse is written as

$$\begin{aligned} J^{-1} &= x_\xi y_\eta z_\zeta + x_\zeta y_\xi z_\eta + x_\eta y_\zeta z_\xi - x_\xi y_\zeta z_\eta \\ &\quad - x_\eta y_\xi z_\zeta - x_\zeta y_\eta z_\xi \end{aligned}$$

The velocity components  $u, v, w$  and the pressure,  $p$ , are related to the total energy per unit volume,  $e$ , through the equation of state for a perfect gas by

$$p = (\gamma - 1)(e - \frac{\rho}{2}(u^2 + v^2 + w^2)) \quad (2)$$

The primitive variables of Eq. (1), viz., the density  $\rho$ , the mass fluxes  $\rho u, \rho v, \rho w$  and the energy per unit volume  $e$ , are normalized by the free stream reference quantities and the pressure  $p$  by  $\gamma p_\infty$ . The reference length and velocity scales are the chord of the blade,  $C$ , and free stream speed of sound,  $a_\infty$ , respectively. The details of the metrics of transformation  $(\xi_t, \xi_x, \xi_y, \xi_z)$ ,  $(\eta_t, \eta_x, \eta_y, \eta_z)$  and  $(\zeta_t, \zeta_x, \zeta_y, \zeta_z)$  can be found in Ref. 13.

In the above equations  $u, v$ , and  $w$  are the Cartesian components of velocity in the inertial coordinate system  $(x, y, z, t)$ . In the present formulation Eq. (1) is solved in

the inertial frame of reference with the boundary conditions applied on the rotating blade. The inertial coordinates  $\mathbf{X} = (x, y, z, t)$  are related to the blade-fixed coordinates  $\mathbf{X}_b = (\bar{x}, \bar{y}, \bar{z})$  through the relation given by

$$\begin{aligned} \mathbf{X}(x, y, z, t) &= \mathbf{R}(\bar{t})\mathbf{X}_b(\bar{x}, \bar{y}, \bar{z}) \\ t &= \bar{t} \end{aligned} \quad (3)$$

where  $\mathbf{R}(t)$  is the rotational matrix<sup>14</sup> given by

$$R(t) = \begin{bmatrix} \cos \Omega \bar{t} & -\sin \Omega \bar{t} & 0 \\ \sin \Omega \bar{t} & \cos \Omega \bar{t} & 0 \\ 0 & 0 & 1 \end{bmatrix} \quad (4)$$

Here  $\Omega$  is the angular velocity of the rotor and  $\Omega t$  represents the azimuth sweep of the rotor blade.

The equations set, Eq. (1), is solved using a two-factor, implicit, finite-difference numerical scheme, developed by Ying et al.,<sup>15</sup> that uses spatial central-differencing in the  $\eta$  and  $\zeta$  directions and upwind-differencing in the  $\xi$  direction and is given by

$$\begin{aligned} &[I + h\delta_\xi^b(\widehat{A}^+)^n + h\delta_\zeta \widehat{C}^n - hRe^{-1}\bar{\delta}_\zeta J^{-1}\widehat{M}^n J - D_i|_\zeta] \\ &\times [I + h\delta_\xi^f(\widehat{A}^-)^n + h\delta_\eta \widehat{B}^n - D_i|_\eta] (\Delta \widehat{Q}^n - \Delta \widehat{Q}_o^n) = \\ &- \Delta t \{ \delta_\xi^f [(\widehat{F}^+)^n - \widehat{F}_o^+] + \delta_\xi^f [(\widehat{F}^-)^n - \widehat{F}_o^-] \\ &+ \delta_\eta (\widehat{G}^n - \widehat{G}_o) + \delta_\zeta (\widehat{H}^n - \widehat{H}_o) - Re^{-1}\bar{\delta}_\zeta (\widehat{S}_\zeta^n) \} \\ &- (D_e|_\eta + D_e|_\zeta)(\widehat{Q}^n - \widehat{Q}_o^n) \end{aligned} \quad (5)$$

where  $h = \Delta t$  for first-order time accuracy. Here  $\delta$  is typically a three-point, second-order-accurate, central difference operator,  $\bar{\delta}$  is a midpoint operator used with the viscous terms, and the operators  $\delta_\xi^b$  and  $\delta_\xi^f$  are backward and forward three-point difference operators. The time index is denoted by  $n$  such that  $t = (n\Delta t)$ , and  $\Delta \widehat{Q}^n = \widehat{Q}^{n+1} - \widehat{Q}^n$ . The flux vector  $\widehat{F}$  has been split into  $\widehat{F}^+$  and  $\widehat{F}^-$ , according to its eigenvalues,<sup>16</sup> and the matrices  $\widehat{A}^\pm$ ,  $\widehat{B}$ ,  $\widehat{C}$ , and  $\widehat{M}$  result from the local linearization of fluxes about the previous time level (see Ref. 13). The finite-difference scheme described in Eq. (5) uses flux-splitting in  $\xi$  direction and central differencing in the  $\eta$  and  $\zeta$  directions. As a consequence, numerical dissipation terms denoted by  $D_i$  and  $D_e$  are employed in the  $\eta$  and  $\zeta$  directions, and are given as combinations of second- and fourth-differences. In the vicinity of shock waves, the fourth-difference terms can cause oscillations, so it is desirable to drop these terms and rely only on the second-difference terms.

The factored operators are solved by sweeping in the  $\xi$  direction and inverting tridiagonal matrices with  $5 \times 5$  blocks for the other two directions. Currently, a significant part of the computational time is taken to form the plus and minus Jacobian matrices for the flux vector  $\hat{F}$  with this numerical scheme. However, this effort has been reduced by computing  $\hat{A}^+$  and  $\hat{A}^-$  at every other point (in both  $\eta$  and  $\zeta$  directions) and averaging to obtain the matrices at the intermediate points. The numerical code is vectorized for the Cray-2 supercomputer.

In writing Eq. (5) it is assumed that  $\hat{A}_0^\pm \approx \hat{A}^\pm$ ,  $\hat{B}_0 \approx \hat{B}$ , and  $\hat{C}_0 \approx \hat{C}$  where the Jacobian matrices  $\hat{A}_0^\pm$ ,  $\hat{B}_0$  and  $\hat{C}_0$  correspond to the prescribed-vortex flowfield. In the absence of vortex interaction, the prescribed-disturbance flowfield reduces to a free stream.

In using this numerical algorithm for the physical problem presented here, a note of caution is in order. As noted before, the numerical scheme is second-order accurate in space. Although it is desirable to have higher-order accuracy in space, it turns out that the present algorithm is numerically more stable if this accuracy is decreased slightly from the second-order. Also, in evaluating the right hand side of Eq. (5), it is desirable to calculate the derivatives of individual fluxes first and then taking a difference. This is particularly true for the fluxes in the  $\zeta$  direction.

A body-conforming finite-difference grid has been used for the rectangular blade having an aspect ratio of 7 and consists of a warped spherical O-O grid topology. The flowfield grid is generated using the three-dimensional hyperbolic grid solver of Steger and Chaussee<sup>17</sup> with proper clustering in the leading and trailing edge regions and in the tip region. The grid is nearly orthogonal at the surface and the spacing in the normal direction at the surface is chosen to be  $0.0002C$  for the viscous grid and  $0.02C$  for the Euler grid. The viscous computations are done on a grid consisting of 21 points along the span, 101 in the periodic direction around the blade and 31 in the normal direction. The Euler grid is more coarser with only  $21 \times 101 \times 15$  grid points. The outer grid boundary was chosen to be at 8 chords in all directions for both viscous and inviscid grids.

The boundary conditions, both surface and farfield, are applied explicitly. At the rotating blade surface because of the noslip condition for viscous flows, the contravariant velocities  $U$ ,  $V$  and  $W$  are set to zero. However, the surface velocity in the inertial frame is nonzero since it is equal to the surface grid velocity, determined by the time metrics  $\xi_t$ ,  $\eta_t$  and  $\zeta_t$  as the blade (and the grid attached to it) moves in azimuth. The Euler calculations use an extrapolation of contravariant velocities to the surface. The

density at the wall is determined by zeroth-order extrapolation. The pressure along the body surface is calculated from the normal momentum relation (see, for example Ref. 13). Having calculated the density and pressure, the total energy is determined from the equation of state.

At the farfield boundary the flow quantities are either fixed or extrapolated from the interior depending on whether the flow is subsonic or supersonic and if it is of inflow- or outflow-type at the boundary. The characteristic velocities of the Euler equations determine the number of flow properties to be specified to control the reflections of waves from the boundaries. For the subsonic-inflow boundary, four quantities must be specified and one quantity is determined. The four specified here are a Riemann invariant, the entropy, and two tangential velocities; the quantity that is calculated is also a Riemann invariant. For the supersonic-inflow, all flow quantities are specified. At the subsonic-outflow boundaries, only one quantity is specified. For the supersonic-outflow condition all flow quantities are extrapolated from the interior. The plane containing the blade root is chosen very close to the rotation axis of the blade (at  $R = 1.0C$ ) and is also treated as a farfield boundary.

The interacting line vortex generated upstream of the rotor by a rectangular wing is fixed in the inertial space along a line of constant  $x$ . It is assumed to have an analytical representation for the cylindrical velocity distribution given by

$$v_\theta = \frac{C_k \hat{\Gamma}}{2\pi r} \left( \frac{r^2}{r^2 + a_0^2} \right) \quad (6)$$

The constant  $C_k$  in the above expression has been determined to be equal to 0.8 by matching the peak tangential velocity with the experimentally measured value at the measured radial distance reported in Ref. 2 by Srinivasan et al.<sup>8</sup> The constant  $a_0$  is approximately equal to the radius of the viscous core of the vortex (equal to  $0.167C$  in the present case). The induced velocity due to this line vortex is calculated using the Biot-Savart Law and the pressure field is calculated by solving the radial momentum equation; the vortex is initialized well upstream of the interaction region as described in Ref. 7.

### Results and Discussion

All the calculations performed in this study are done in a time-accurate fashion. The test cases calculated correspond to the two sets of experiments of Caradonna et al.<sup>2,3</sup> for parallel and oblique blade-vortex interactions. Since one of the purposes of the experiments was to collect data

to validate numerical methods, the experimental apparatus was kept simple to ease the representation by numerical methods. The rotor geometry consisted of a two-bladed rigid rotor of approximately 14-chord diameter. The blades have a rectangular planform and consist of an NACA 0012 airfoil with no twist or taper. The rotor blades are essentially nonlifting in the absence of the vortex interaction. The interacting vortex was generated upstream of this rotor by a lifting rectangular wing with an NACA 0015 airfoil. Parallel and oblique BVI are generated by positioning the line vortex along the y-axis ( $x_0 = 0.0$ ) and ahead of the y-axis ( $x_0 < 0.0$ ) so that the rotor blade encounters the vortex on the advancing side in the first- and second-quadrants of the azimuthal travel as shown in Fig. 2.

As mentioned before, the Navier-Stokes hover code described in Ref. 12 provides the starting point for the present investigation. This code has been validated against the experimental data of Caradonna and Tung<sup>18</sup> for the nonlifting and lifting hover conditions at both subcritical and supercritical tip speeds. Although the main focus of the present investigation is to calculate both parallel and oblique blade-vortex interactions, it is necessary to first calculate the base-line rotor-alone flowfield solutions (in the absence of vortex interaction) at the same free stream conditions. Two sets of results for parallel blade-vortex interactions, corresponding to  $M_{tip} = 0.6$  and  $0.8$  and  $\mu = 0.2$  and one set of results for oblique blade-vortex interaction corresponding to  $M_{tip} = 0.763$  and  $\mu = 0.197$ , will be presented in the following sections and compared with experimental data. At the Reynolds numbers corresponding to the blade tip speeds in these experiments, the boundary layer on the entire rotor blade could be assumed to be turbulent and, as mentioned before, an algebraic eddy viscosity model of Baldwin and Lomax<sup>19</sup> is used for calculating the turbulent viscosity.

#### Rotor-Alone Case

The objective of calculating the rotor-alone flowfield solutions serves two purposes. First, it enables an understanding of the importance of unsteady time-lag effects in shock wave growth and decay as well as the three-dimensionality of the flowfield of the advancing rotor, particularly when the flow is supercritical. Second, it provides the baseline solution to eventually calculate the vortex interaction flowfield.

Figure 3 shows the instantaneous surface pressure distributions for various azimuthal positions of the rotor for the case of  $M_{tip} = 0.6$  and  $\mu = 0.2$ . Examination of the results suggests that at this reference station of  $r_B = 0.893$  and for the subcritical flow condition, the flow behaves as if it is quasi-steady and quasi-two-dimensional.

In spite of the gradual increase of the blade-element relative speed in the first quadrant and gradual decrease of the same in the second quadrant, the flowfield appears to remain nearly the same at all azimuth locations (as seen in Fig. 3b) indicating that the unsteady time-lag effects are virtually absent for this flow condition and the flow behaves as if it is quasi-steady. In fact, also shown in Fig. 3b is the quasi-steady solution for one azimuth location of  $\psi = 90^\circ$  which is in perfect agreement with the unsteady solutions at different azimuthal positions. Also, the comparison of three-dimensional results of Fig. 3b with the two-dimensional results<sup>8</sup> of Fig. 3a shows that these results are nearly identical suggesting that the flow also behaves as if it is quasi-two-dimensional.

At the supercritical tip flow conditions, corresponding to  $M_{tip} = 0.8$  and  $\mu = 0.2$ , the basic rotor flowfield is dominated by the presence of a strong shock wave on the advancing blade over large parts of the first- and second-quadrants. For this advancing rotor, the Euler and Navier-Stokes results of instantaneous surface pressures are shown in Fig. 4 at the radial station  $r_B = 0.893$  for different azimuthal positions of the blade. The Euler results show good agreement with the experiments and the Navier-Stokes results have only a qualitative agreement because of coarse grid. It appears that the shock wave position is under predicted for the Navier-Stokes method and slightly over predicted for the Euler method. For this coarse grid solution, the Navier-Stokes method predicts the decay of the shock much faster in the second-quadrant. On the other hand, the Euler method predicts that the shock wave persists at the  $\psi = 180^\circ$  azimuth. Previous two-dimensional Navier-Stokes calculations of the same flow<sup>8</sup> had shown strong three-dimensionality and unsteady time-lags in shock wave growth and decay. The two-dimensional assumption for this flow essentially over-predicted the shock wave position and strength, unlike the subcritical flow condition. In contrast, the three-dimensional Euler results seem to follow the experimental observation correctly.

Thus at this flow condition, the flowfield is highly three-dimensional exhibiting strong unsteady time-lag behaviour in the shock wave formation and eventual demise. The unsteady time-lag feature of the flowfield is demonstrated in the surface pressure distributions of Fig. 4 shown for  $\psi = 60^\circ$  and  $\psi = 120^\circ$  azimuthal positions, which shows that the two results are very different from each other.

In principle, the shock wave should attain its maximum strength when the relative flow speed reaches a maximum value for  $\psi = 90^\circ$  blade azimuthal position. However, the shock wave keeps growing in strength even after the

blade has passed the  $\psi = 90^\circ$  azimuthal position and a weak shock wave seems to persist even at the  $\psi = 180^\circ$  azimuth. The strengthening of the shock wave in the first-quadrant and beyond, and the slow demise of it in the second-quadrant, suggests the existence of a strong unsteady time-lag effect at this flow condition. Such a behavior was totally absent at the subcritical flow condition. The presence of the shock wave seems to introduce not only the time-lag in the adjustment of the flow as the blade sweeps in azimuth, but also makes the flow highly three-dimensional.

In contrast to the flow on the advancing side of the rotor blade, the flowfield of the retreating side appears really benign for this nonlifting rotor. The lingering effects of the shock wave, persisting at  $\psi = 180^\circ$ , soon die out as the blade sweeps into the third-quadrant. Shown in Fig. 5 are the surface pressure distributions for several azimuthal locations of the blade in third- and fourth-quadrants on the retreating cycle. Since the flowfield is basically subcritical on the retreating side, the plots of Fig. 5 appear to have the same behavior as those of Fig. 3.

Figure 6 shows the surface pressure distributions on the advancing rotor at  $r_B = 0.946$  for the flow conditions of  $M_{tip} = 0.763$  and  $\mu = 0.197$ . Since this flow condition is similar to that of the case of Fig. 4, it has the same qualitative behaviour of the flow on the advancing side. As seen in these plots, the Euler calculations are in good agreement with the experimental data.<sup>3</sup> As before, the Navier-Stokes results have only a qualitative agreement for the reasons mentioned before. It is important to mention that the rotor-alone case involves a nonlifting symmetrical blade, for which the pressure distributions should be identical on the upper and lower surfaces. However, the data in Fig. 6, from Ref. 3, seem to have more scatter than the corresponding experimental results from Ref. 2.

#### Quasi-steady vs Unsteady Results

Although the flowfield of a lifting helicopter rotor is, in general, unsteady and three-dimensional, a close inspection of the subsonic surface pressure results presented in Fig. 3b suggests that the unsteady and quasi-steady results are nearly the same for this nonlifting flow condition. In fact, a quasi-steady flow calculated by freezing the rotor blade at certain azimuthal locations (say,  $\psi = 0.0^\circ$ ) produces nearly the same flowfield as an unsteady flowfield irrespective of the flow conditions. In the present approach, the unsteady calculations are started from a baseline quasi-steady solution. At the subcritical flow conditions, similar to that presented in Fig. 3, an unsteady calculation can be started from any azimuthal location of the blade because of the quasi-steady and the unsteady solutions being nearly

identical at all azimuthal locations. However, this is not true for supercritical flow conditions where shock waves are present in the flowfield. For example, Fig. 7 shows the quasi-steady and unsteady surface pressure distributions for the case of  $M_{tip} = 0.8$  and  $\mu = 0.2$  at azimuthal locations of  $\psi = 60^\circ$  and  $120^\circ$ . For this flow condition, these results indicate that the quasi-steady assumption overpredicts the shock strength at  $\psi = 60^\circ$  and underpredicts at  $\psi = 120^\circ$ . Nevertheless, at  $\psi = 0.0^\circ$  position, the quasi-steady and unsteady results are nearly identical even for this flow condition. So, for flow conditions that are severe, it is still reasonable to start the unsteady marching from the quasi-steady solution calculated at  $\psi = 0.0^\circ$  azimuthal location.

#### Parallel Blade-Vortex Interaction

During the unsteady three-dimensional close encounter of a curved tip vortex with a rotating blade, the helicopter rotor undergoes a variety of blade-vortex interactions depending on the interaction angle between the leading edge of the rotating blade and the curved line vortex. These interactions are generally unsteady and three-dimensional. One limiting case of such an encounter, for zero interaction angle, is termed parallel interaction (see, for example, Ref. 7). In the experimental configuration considered here, this interaction occurs around  $\psi = 180^\circ$  azimuthal position. For an observer riding with the blade (at a given reference station along the span), it appears as though the observer is passing a fixed vortex in the flow. For of this reason, this interaction is sometimes approximated as two-dimensional and unsteady.

To calculate accurately the blade-vortex interaction flowfield, it is necessary to preserve the vortex structure without numerical diffusion. As mentioned before, one method that has been demonstrated to work effectively and economically in achieving this is the prescribed-disturbance scheme.<sup>7</sup> The effectiveness of this scheme is illustrated in Fig. 8 (reproduced from Ref. 20) showing the variation of lift coefficient as a function of vortex location during an airfoil-vortex interaction. Also shown in this figure is the Euler lift distribution calculated using a conventional (vortex capturing) technique.<sup>21</sup> Although the two Euler solutions are computed on the same grid, the numerical dissipation associated with the finite grid-spacing progressively weakens the gradients and reduces the effective vortex strength in the conventional method. Also, this numerical error is grid-dependent (the finer the grid the lesser the error); however, it is completely absent in the prescribed-vortex solutions, which are essentially independent of the grid. Hence, the prescribed-disturbance method has been used here for preserving the vortex

structure.

### Subcritical Interaction

The results of a subcritical parallel BVI are discussed here. This case corresponds to the flow conditions of  $M_{tip} = 0.6$ ,  $\mu = 0.2$ , and  $C_k \hat{\Gamma} = 0.133$  at a blade reference station (marked AA in Fig.2)  $r_B = 0.893$ . The interacting vortex is located at  $x_o = 0.0$  and  $z_o = -0.4$  along the  $y$ -axis. To calculate the BVI flowfield, the interacting vortex is initialized with the baseline rotor solution at the azimuthal position of  $\psi = 120^\circ$ . The unsteady flow field is monitored as the blade continues to advance in azimuth, and the peak interaction effects are shown in Fig. 9 in the form of instantaneous surface pressure distributions measured around  $\psi = 180^\circ$  azimuthal position.

The present Euler results are in very good agreement with both the experimental data<sup>2</sup> and a previous two-dimensional Navier-Stokes calculation<sup>8</sup>. As seen from Fig. 9a for  $\psi = 178.15^\circ$  the lift on the blade, which is initially zero in the absence of vortex interaction, is negative (because of the sense of rotation of vortex) and gradually becomes positive as the blade passes the line vortex. This crossover of lift, from negative to positive, seems to occur when the vortex is approximately aligned with the quarter-chord line of the blade (corresponding to  $\bar{x}_v = 0.0$ ). As mentioned before, the two-dimensional approximation of this three-dimensional, unsteady interaction is, in fact, a very good assumption for this subcritical flow condition. The close agreement of the viscous and inviscid results suggests that the viscous effects are unimportant for this relatively weak interaction.

### Supercritical Interaction

This case corresponds to the flow condition of  $M_{tip} = 0.8$ ,  $\mu = 0.2$ , and  $C_k \hat{\Gamma} = 0.177$  at a blade reference station of  $r_B = 0.893$ . The interacting vortex location is same as in subcritical case. This flow condition, in contrast to the subcritical flow condition, exhibits strong unsteady time-lag effects in shock wave growth and decay for the advancing rotor. This feature seems to accentuate the three-dimensional nature of the flow and a two-dimensional approximation of this flow over predicts the shock wave strength and location as demonstrated in Ref. 8.

As before, to calculate the BVI flowfield, the interacting vortex is initialized at about  $\psi = 120^\circ$  azimuthal position and the time evolution of the flow is monitored as the blade advances in azimuth. Figures 10-11 show the interaction flowfield results in terms of instantaneous surface pressures for several azimuthal positions of the blade for the Euler and the Navier-Stokes calculations. Also shown

in this figures are the experimental data<sup>2</sup>. Comparison of the results shows that while the Euler results (Fig. 10) have good agreement with the experimental data for all azimuthal locations of the blade, the Navier-Stokes results (Fig. 11) show only a qualitative agreement with the experimental data. This feature is strongly dependent on the accuracy of the base-line solution at the azimuthal location where the vortex is initialized. The vortex is initialized at the  $\psi = 120^\circ$  position of the blade for this case. Comparison of surface pressures of Fig. 4d at this location for the Navier-Stokes and Euler calculations shows that the Euler results have better agreement with experiments than the Navier-Stokes results. Although the Euler grid is very coarse, it seems to capture the essential details of the flow sharply including the shock waves. Since the Navier-Stokes grid is too coarse, the shocks appear smeared. Nevertheless, it captures the essential qualitative features of the flow.

The effect of vortex interaction is to induce time dependent aerodynamic forces on the rotor. For example, as seen from the surface pressure plots of Figs. 10-11, the lift on the blade, which is initially zero, becomes negative (because of the sense of rotation of vortex) due to induced downwash and gradually increases to a positive value as the blade passes the fixed vortex. The peak effects of the interaction appear to occur when the blade leading edge is approximately above the line vortex.

### Oblique Blade-Vortex Interaction

This case corresponds to a free stream condition of  $M_{tip} = 0.763$  and  $\mu = 0.197$ . The interacting vortex located at  $x_o = -2.13$  and  $z_o = -0.25$  has a strength of  $C_k \hat{\Gamma} = 0.179$  for the reference blade section at  $r_B = 0.946$ . In contrast to the parallel interaction, the oblique interaction occurs over a larger azimuthal sweep of the rotor blade starting in first-quadrant and completing in second-quadrant. The peak interaction occurs at around  $\psi = 20^\circ$  in the first-quadrant and around  $\psi = 160^\circ$  in the second-quadrant. Therefore, the vortex is initialized at  $\psi = 0.0^\circ$  and the evolution of the unsteady interacting flow is monitored for the advancing rotor.

Figures 12-13 show the surface pressure distributions for several azimuthal positions of the blade from the Euler and the Navier-Stokes calculations of the interaction flowfield. As observed before, the transonic Euler calculations agree better with the experimental data<sup>3</sup> than the Navier-Stokes calculations for the reasons cited earlier. On the other hand, the interaction in the first-quadrant occurs at subcritical flow condition and therefore the agreement of both the Euler and Navier-Stokes calculations with the experimental data is good at  $\psi = 50^\circ$ . For the interaction

in the second-quadrant, where the flow is supercritical, the Euler results have better agreement with the experiments than the Navier-Stokes results. Compared to the preceding transonic *parallel* interaction results, the Navier-Stokes results for this interaction appear to agree better with the experimental data. This is in direct consequence of the better agreement of the rotor-alone Euler and the Navier-Stokes surface pressures at all azimuthal positions, as seen in Fig. 12 for this flow condition. The maximum relative blade tip speed in this case (for  $\psi = 90^\circ$  position) is 0.91 compared to a value of 0.96 corresponding to the transonic parallel interaction case and is thus a weaker interaction.

From the surface pressures of Fig. 13, it can be seen that the lift on rotor blade, which is initially zero, becomes negative due to the vortex influence (because of the sense of rotation), increases to a maximum (negative) value in second-quadrant, and changes over to a positive value at about  $\psi = 165^\circ$  azimuthal position of the blade. The peak interaction appears to occur around the  $\psi = 160^\circ$  azimuthal position.

### Conclusions

A numerical procedure is presented to calculate the unsteady, viscous and inviscid, three-dimensional flowfields of a helicopter rotor in forward flight and parallel and oblique blade-vortex interactions in subcritical and supercritical flow conditions. Important flow features such as unsteady time-lag effects in shock wave growth and demise, as well as the importance of three-dimensional effects are discussed. While it is possible, under certain flow conditions, to approximate the parallel blade-vortex interaction as two-dimensional and unsteady, the oblique blade-vortex interaction, on the other hand, is naturally three-dimensional, and unsteady and has to be treated that way without any simplifications.

The numerical results are compared with two-sets of test data generated by Caradonna et al.<sup>2,3</sup> on a model two-bladed rotor in a wind tunnel. While the Euler results have good agreement with experiments, the Navier-Stokes results, with a coarse grid, have only a good qualitative agreement. Nevertheless, the study demonstrates that the numerical methodology presented here is capable of calculating accurately the flowfield of a helicopter rotor including the effects of vortex interaction under subcritical and supercritical flow conditions.

### Acknowledgements

The first author (GRS) would like to acknowledge the support of this research by the U. S. Army Research Office under Contract DAAL03-88-C-0006. Computational time was provided by the Applied Computational Fluids Branch of NASA Ames Research Center. The authors would like

to thank Dr. J. L. Steger for some stimulating discussions.

### References

1. Srinivasan, G. R., McCroskey, W. J., Baeder, J. D., and Edwards, T. A., "Numerical Simulation of Tip Vortices of Wings in Subsonic and Transonic Flows", AIAA Journal, Vol. 26, No. 10, October 1988, pp. 1153-1162.
2. Caradonna, F. X., Laub, G. H., and Tung, C., "An Experimental Investigation of the Parallel Blade-Vortex Interaction", Paper presented at the 10th European Rotorcraft Forum, The Hague, Netherlands, August 1984.
3. Caradonna, F. X., Lautenschlager, J., and Silva, M., "An Experimental Study of Rotor Blade-Vortex Interactions", AIAA Paper 88-0045, January 1988.
4. Workshop on Blade-Vortex Interactions (unpublished), NASA Ames Research Center, Moffett Field, California, October 1984.
5. Rai, M. M., "Navier-Stokes Simulation of Blade-Vortex Interaction Using High-Order Accurate Upwind Schemes", AIAA Paper 87-0543, January 1987.
6. Steinhoff, J. and Suryanarayanan, K., "The Treatment of Vortex Sheets in Compressible Potential Flow", AIAA Paper 83-1881-CP, July 1983.
7. Srinivasan, G. R. and McCroskey, W. J., "Numerical Simulations of Unsteady Airfoil-Vortex Interactions", VERTICA, Vol. 11, 1987, pp. 3-28.
8. Srinivasan, G. R., McCroskey, W. J., and Baeder, J. D., "Aerodynamics of Two-Dimensional Blade-Vortex Interaction", AIAA Journal, Vol. 24, No. 10, October 1986, pp. 1569-1576.
9. Wu, J. C., Sankar, N. L., and Hsu, T. M., "Unsteady Aerodynamics of an Airfoil encountering a Passing Vortex", AIAA Paper 85-0203, January 1985.
10. Strawn, R. C. and Tung, C., "The Prediction of Transonic Loading on Advancing Helicopter Rotors", NASA TM-88238, April 1986.
11. Caradonna, F. X., Strawn, R. C., and Bridgeman, J.O., "An Experimental and Computational Study of Rotor-Vortex Interactions", paper presented at the Fourteenth European Rotorcraft Forum, Milano, Italy, September 1988.
12. Srinivasan, G. R. and McCroskey, W. J., "Navier-Stokes Calculations of Hovering Rotor Flowfields", Journal of Aircraft, Vol. 25, No. 10, October 1988, pp. 865-874.
13. Pulliam, T. H. and Steger, J. L., "Implicit Finite-

Difference Simulations of Three-Dimensional Compressible Flow", AIAA Journal, Vol. 18, No. 2, February 1980, pp. 159-167.

14. Isom, M. P., "Unsteady Subsonic and Transonic Potential Flow Over Helicopter Rotor Blades", NASA CR-2463, October 1974.

15. Ying, S. X., Steger, J. L., Schiff, L. B., and Baganoff, D., "Numerical Simulation of Unsteady, Viscous, High-Angle-Of-Attack Flows Using a Partially Flux-Split Algorithm", AIAA Paper 86-2179, August 1986.

16. Steger, J. I. and Warming, R. F., "Flux Vector Splitting of the Inviscid Gasdynamic Equations with Application to Finite-Difference Methods", J. of Comp. Phys., Vol. 40, No.2, 1981, pp.263-293.

17. Steger, J. L. and Chaussee, D. S., "Generation of Body-Fitted Coordinates Using Hyperbolic Partial Differential Equations", SIAM J. Sci. Stat. Comput., Vol. 1, No. 4, December 1980, pp. 431-437.

18. Caradonna, F. X. and Tung, C., "Experimental and Analytical Studies of a Model Rotor in Hover", VERTICA, Vol. 5, No. 2, 1981, pp. 149-161.

19. Baldwin, B. S. and Lomax, H., "Thin Layer Approximation and Algebraic Model for Separated Turbulent Flow", AIAA Paper 78-257, January 1978.

20. McCroskey, W. J. and Srinivasan, G. R., "Unsteady Interactions of Transonic Airfoils with Gusts and Concentrated Vortices", AGARD-CP-386, Unsteady Aerodynamics-Fundamentals and Applications to Aircraft Dynamics, November 1985, pp. S2.1 - S2.13.

21. Srinivasan G. R., Chyu W. J. and Steger J. L., "Computation of Simple Three-Dimensional Wing-Vortex Interaction in Transonic Flow", AIAA Paper 81-1206, June 1981.

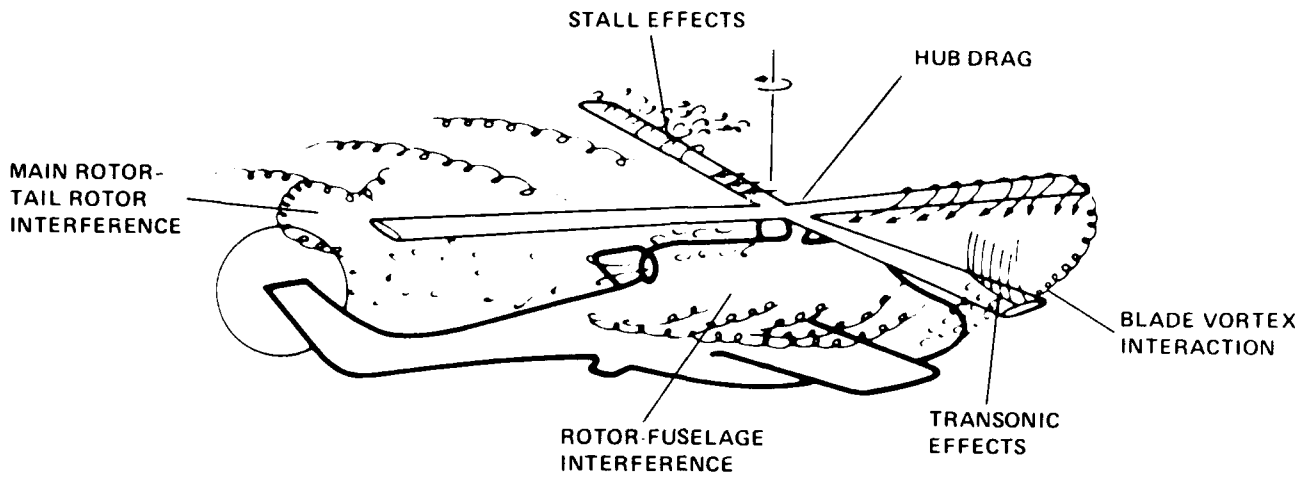


Fig. 1 Schematic of the complex flowfield of a helicopter rotor in forward flight.

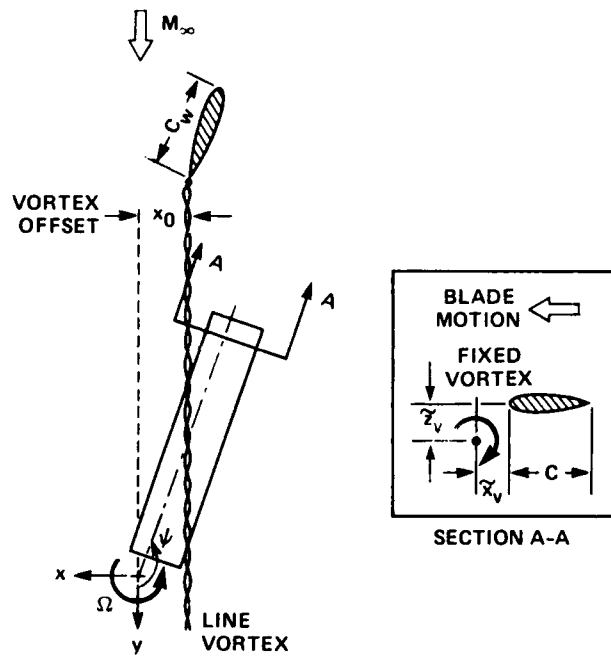


Fig. 2 Schematic of the rotor BVI wind tunnel test.

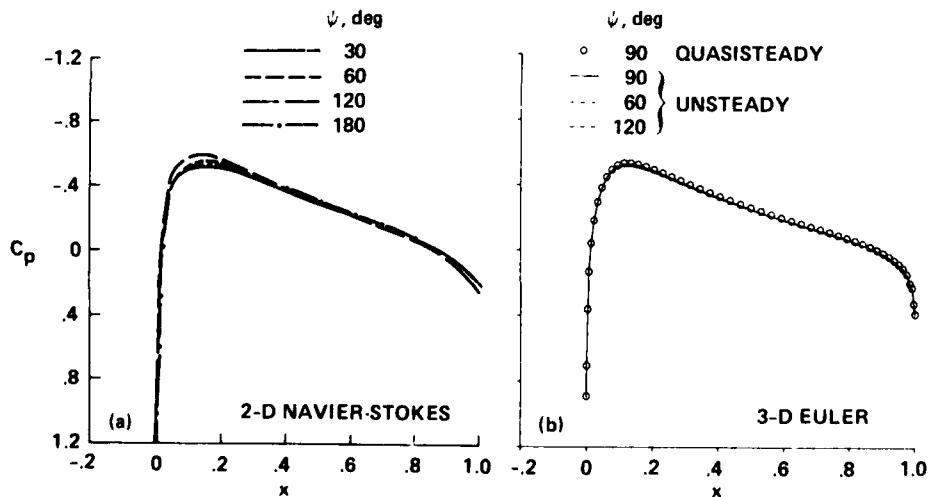


Fig. 3 Instantaneous surface pressure distributions at the reference blade section for advancing rotor.  $M_{tip} = 0.6$ ,  $\mu = 0.2$ ,  $Re = 2.1 \times 10^6$ ,  $r_B = 0.893$ .

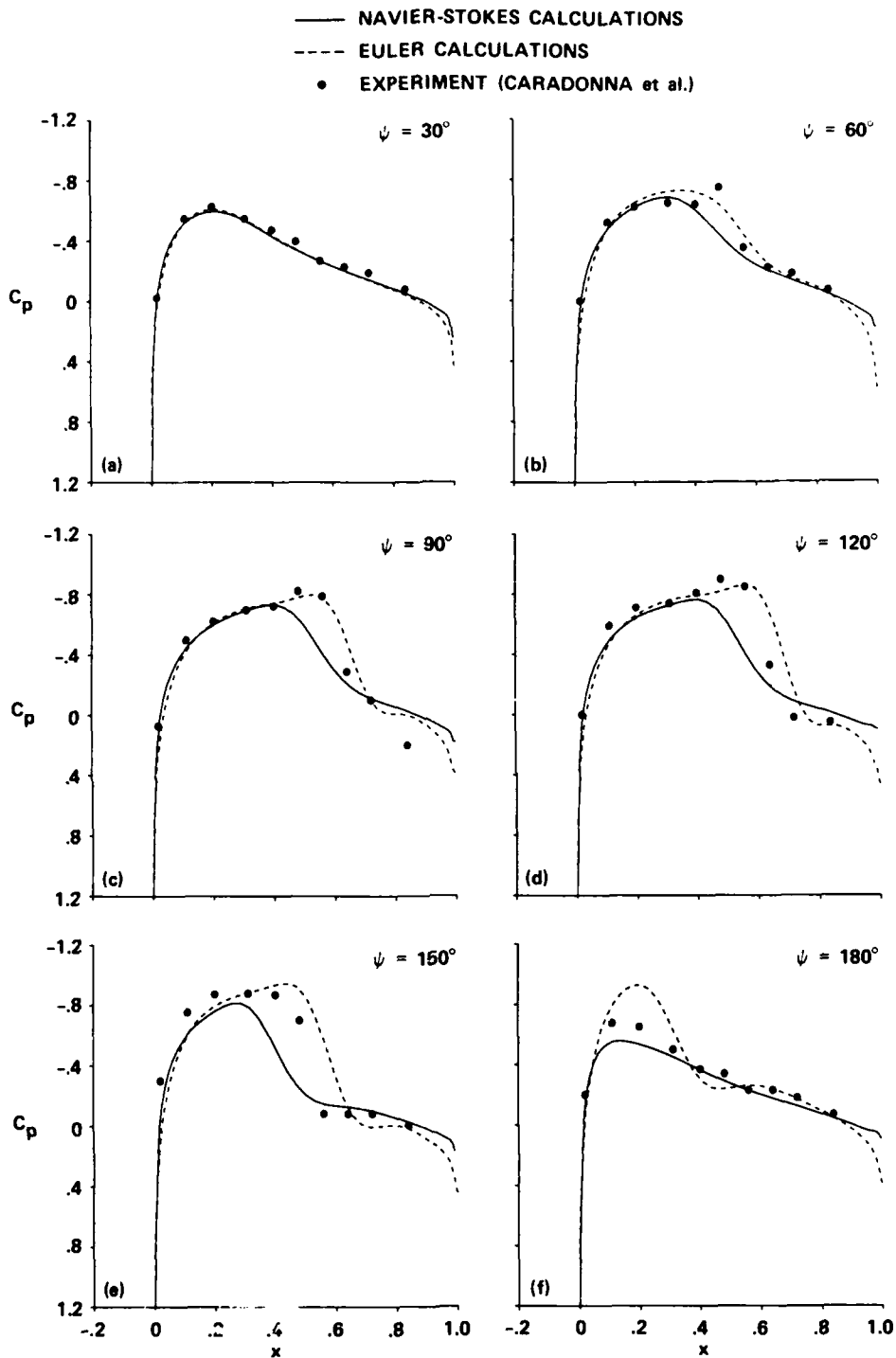


Fig. 4 Instantaneous surface pressure distributions at the reference blade section for advancing rotor.  $M_{tip} = 0.8$ ,  $\mu = 0.2$ ,  $Re = 2.89 \times 10^6$ ,  $r_B = 0.893$ .

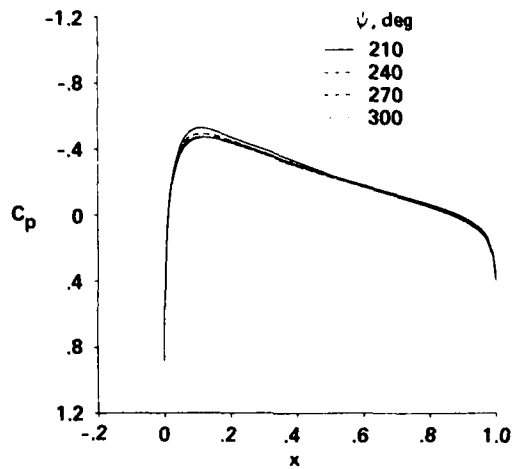


Fig. 5 Instantaneous surface pressure distributions at the reference blade section for retreating blade-Euler solution.  $M_{tip} = 0.8$ ,  $\mu = 0.2$ ,  $r_B = 0.893$ .

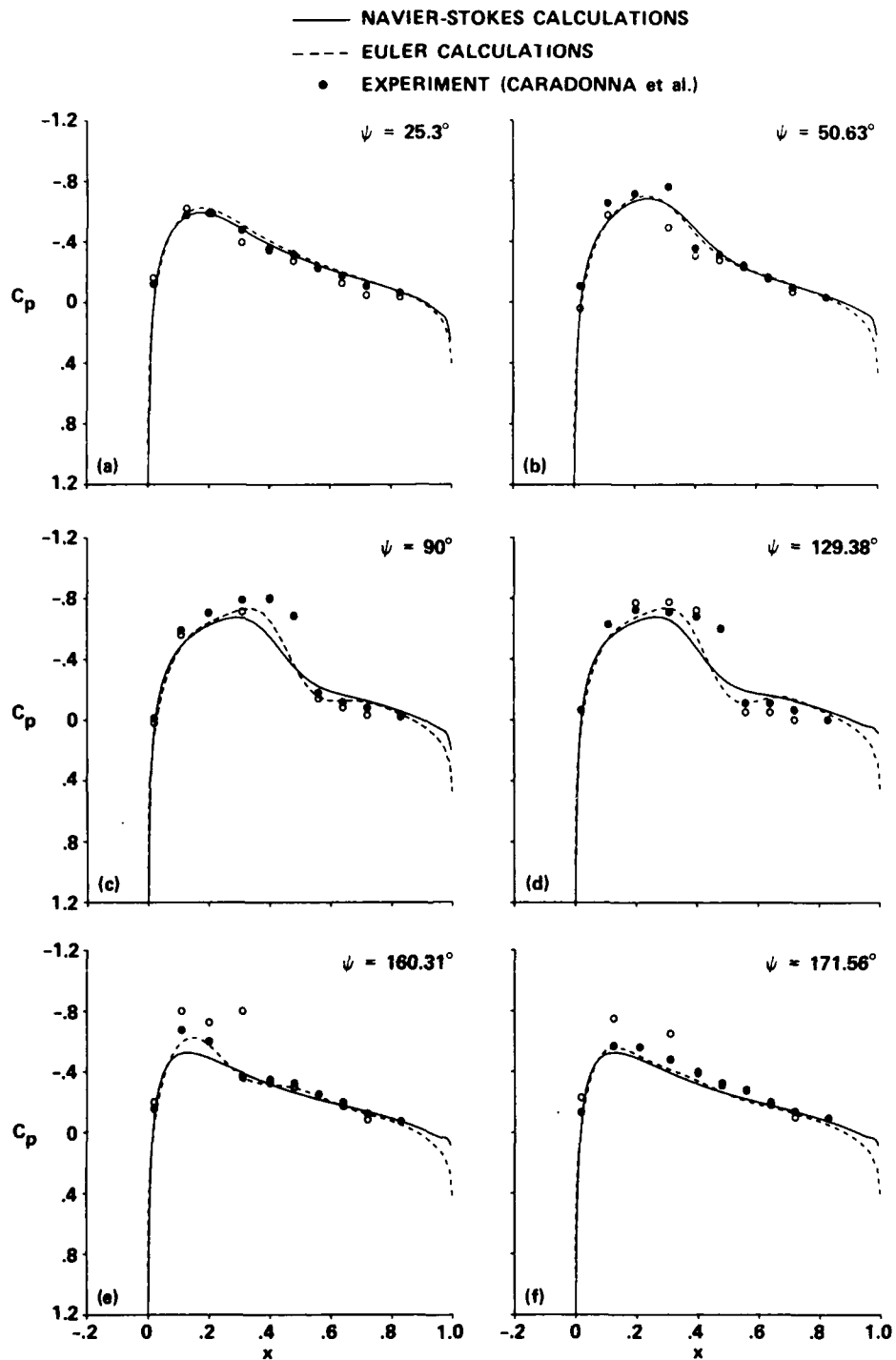


Fig. 6 Instantaneous surface pressure distributions at the reference blade section for advancing rotor.  $M_{tip} = 0.763$ ,  $\mu = 0.197$ ,  $Re = 2.75 \times 10^6$ ,  $r_B = 0.946$ .

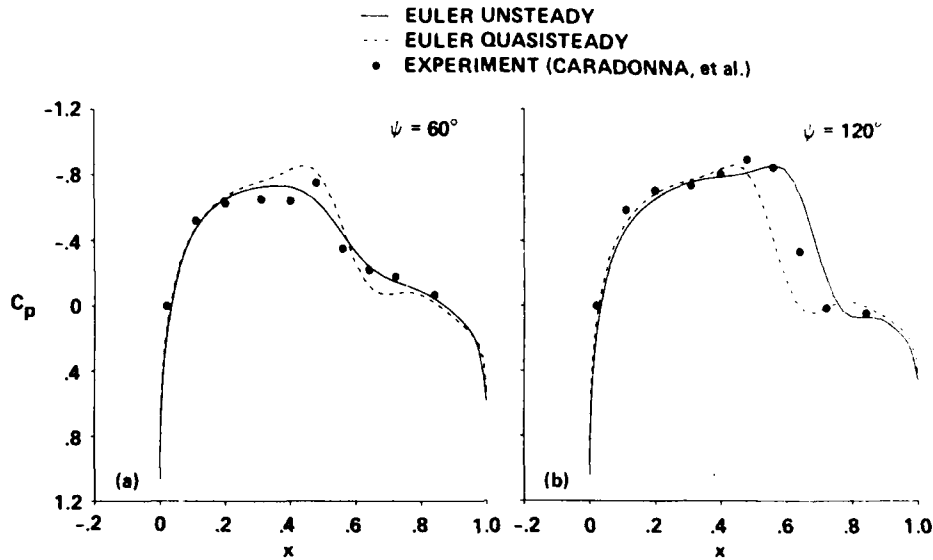


Fig. 7 Comparison of pressure distributions for quasi-steady and unsteady Euler calculations.  $M_{tip} = 0.8$ ,  $\mu = 0.2$ ,  $r_B = 0.893$ .

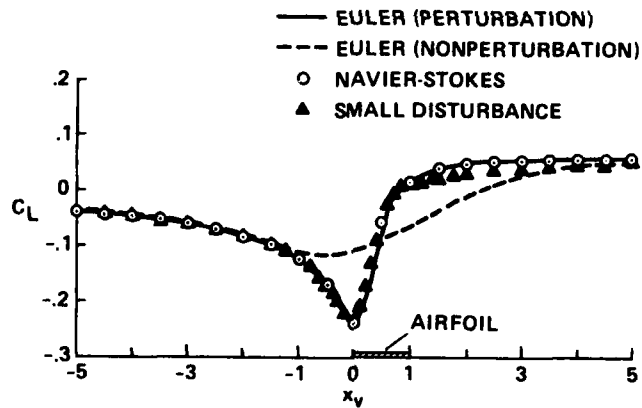


Fig. 8 Effectiveness of the prescribed-vortex method for two-dimensional BVI: NACA 64A006 airfoil.  $M_\infty = 0.85$ ,  $\hat{\Gamma} = 0.2$ ,  $z_o = -0.26$ . (Reproduced from Ref. 20.)

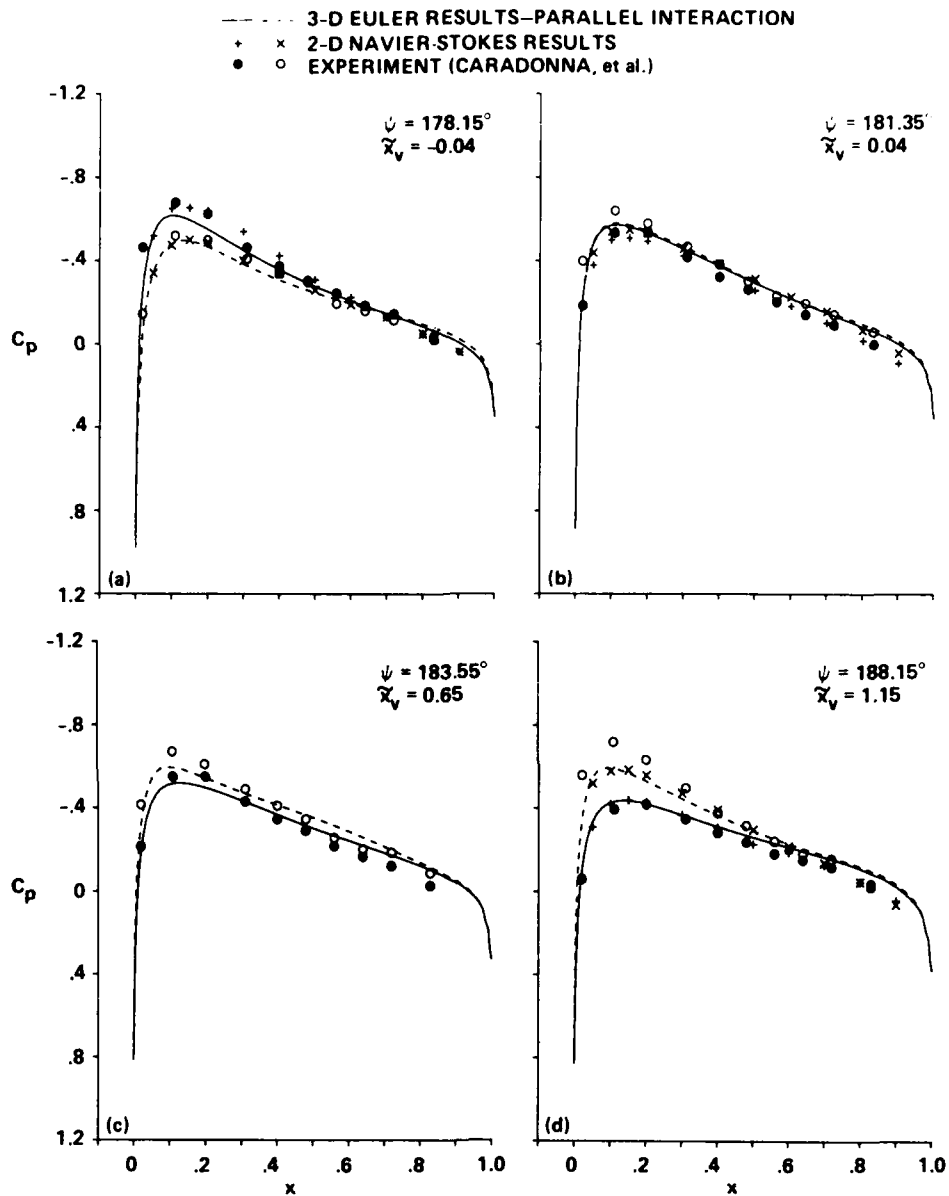
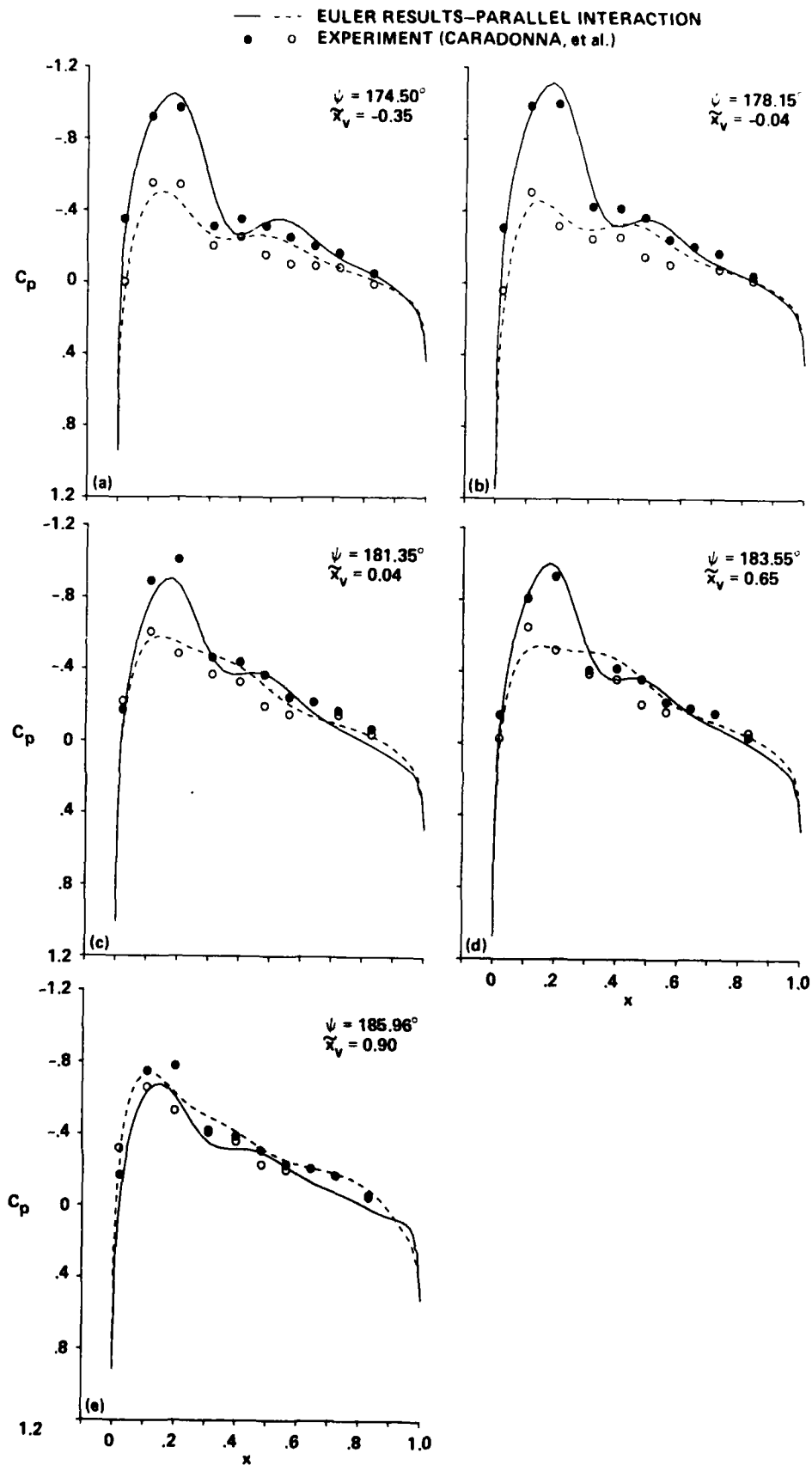


Fig. 9 Comparison of instantaneous surface pressures during subsonic parallel blade-vortex interaction. The solid line, the solid circle, and the symbol + refer to the vortex side of the blade.  $M_{tip} = 0.6$ ,  $\mu = 0.2$ ,  $Re = 2.1 \times 10^6$ ,  $\hat{\Gamma} = 0.133$ ,  $x_o = 0.0$ ,  $z_o = -0.4$ ,  $r_B = 0.893$ .



**Fig. 10 Instantaneous surface pressures during transonic parallel blade-vortex interaction - the Euler results. The solid line and the solid circle refer to the vortex side of the blade.  $M_{tip} = 0.8$ ,  $\mu = 0.2$ ,  $\hat{\Gamma} = 0.177$ ,  $x_o = 0.0$ ,  $z_o = -0.4$ ,  $r_B = 0.893$ .**

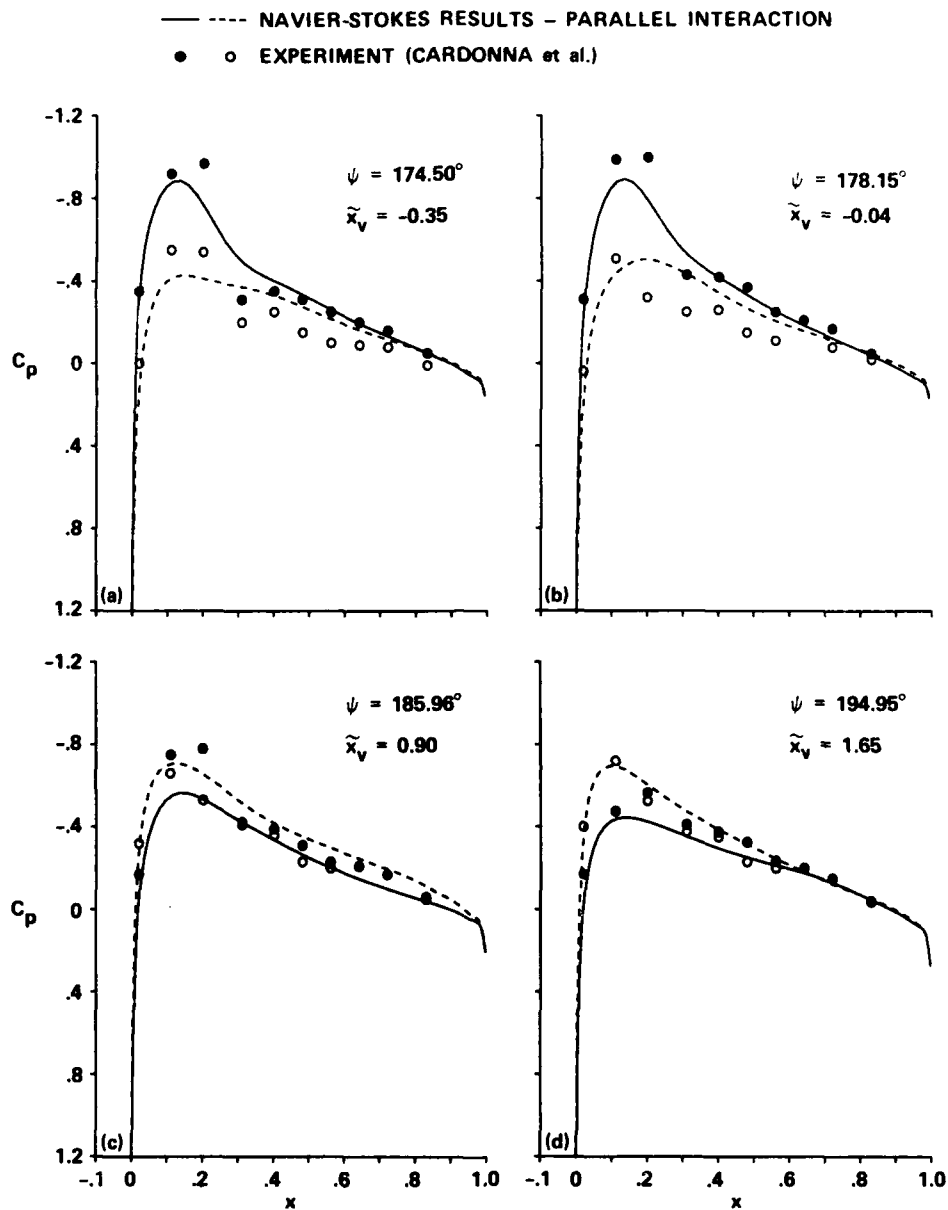


Fig. 11 Instantaneous surface pressures during parallel blade-vortex interaction - the Navier-Stokes results. The solid line and the solid circle refer to the vortex side of the blade.  $M_{tip} = 0.8$ ,  $\mu = 0.2$ ,  $Re = 2.89 \times 10^6$ ,  $\hat{\Gamma} = 0.177$ ,  $x_o = 0.0$ ,  $z_o = -0.4$ ,  $r_B = 0.893$ .

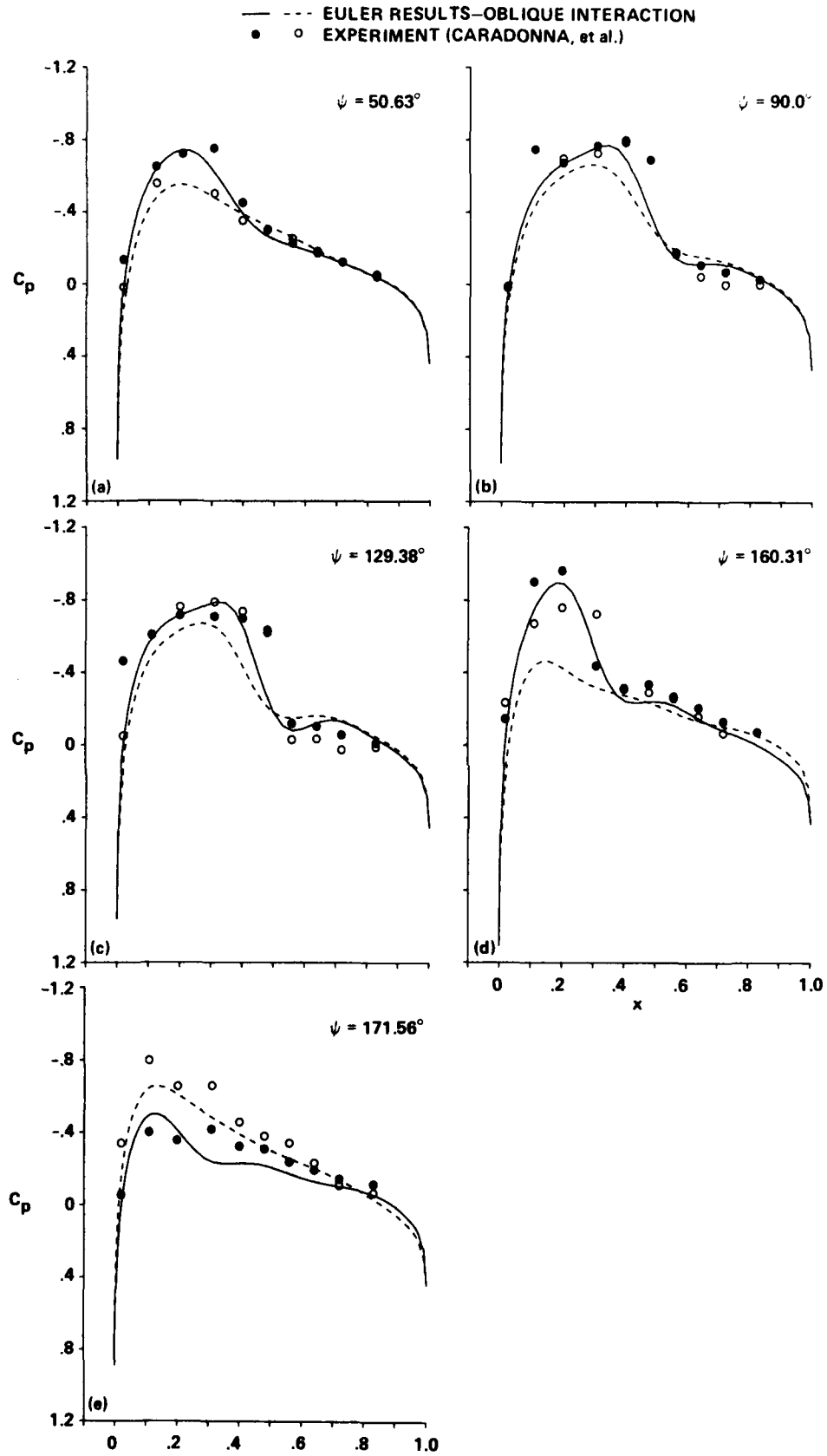


Fig. 12 Instantaneous surface pressures during oblique blade-vortex interaction - the Euler results. The solid line and the solid circle refer to the vortex side of the blade.  $M_{tip} = 0.763$ ,  $\mu = 0.197$ ,  $Re = 2.75 \times 10^6$ ,  $\hat{\Gamma} = 0.179$ ,  $x_o = -2.13$ ,  $z_o = -0.25$ ,  $r_B = 0.946$ .

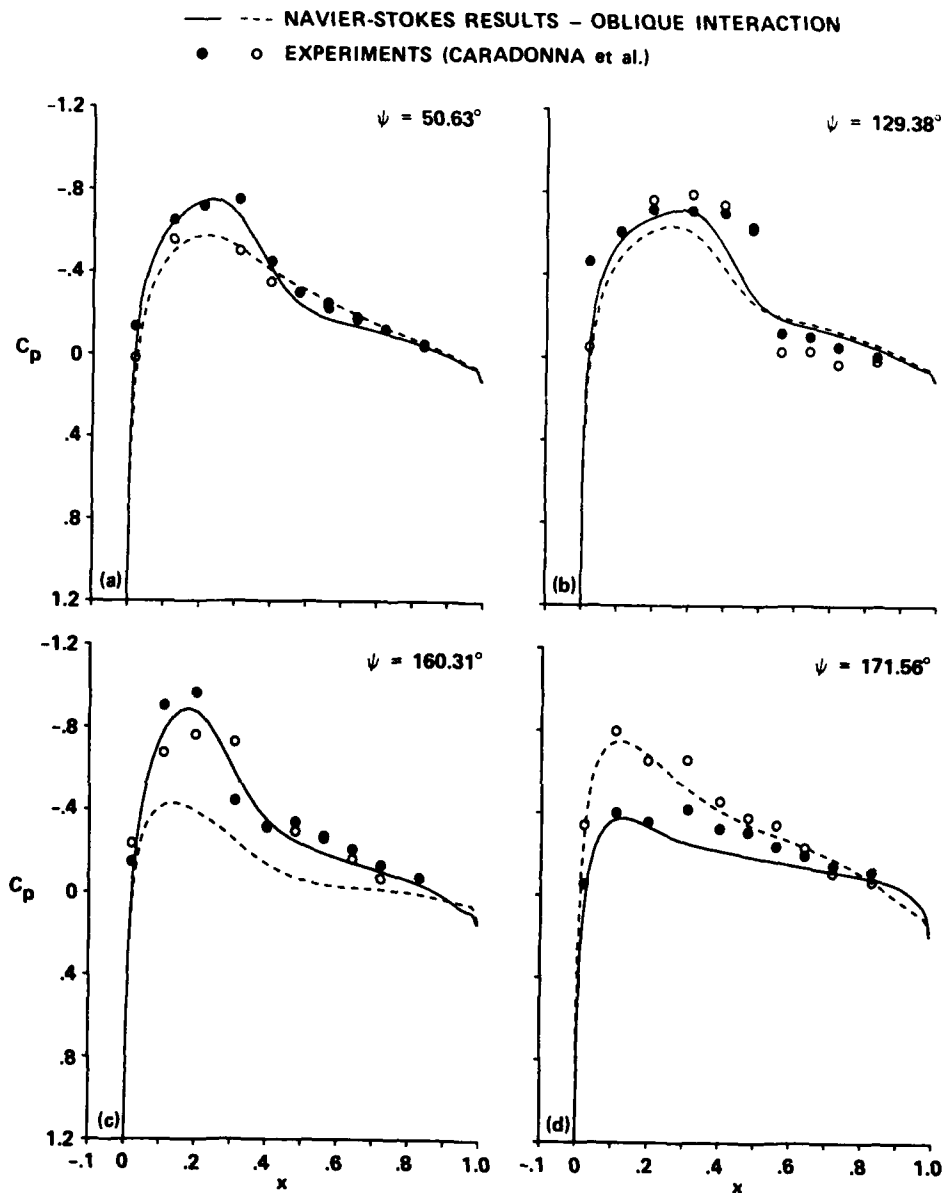


Fig. 13 Instantaneous surface pressures during oblique blade-vortex interaction - the Navier-Stokes results. The solid line and the solid circle refer to the vortex side of the blade.  $M_{tip} = 0.763$ ,  $\mu = 0.197$ ,  $Re = 2.75 \times 10^6$ ,  $\Gamma = 0.179$ ,  $x_o = -2.13$ ,  $z_o = -0.25$ ,  $r_B = 0.946$ .